KURENAI

Kyoto University Research Information Repository

KYOTO UNIVERSITY

| Title | Effects of a Macro-Roughness Element on Tsunami Wave Amplification, Pressures, and Loads: Physical Model and Comparison to Japanese and US Design Equations |
|---|---|
| Author(s) | Tomiczek, Tori; Prasetyo, Adi; Mori, Nobuhito; Yasuda, Tomohiro; Kennedy, Andrew |
| Citation | Coastal Engineering Journal (2017), 59(1) |
| Issue Date | 2017-03 |
| URL | http://hdl.handle.net/2433/219473 |
| Right | ©The Author(s) This is an Open Access article published by World Scientific Publishing Company. It is distributed under the terms of the Creative Commons Attribution 4.0 (CC-BY) License. Further distribution of this work is permitted, provided the original work is properly cited. |
| Type | Journal Article |
| Textversion | publisher |

Kyoto University

# Effects of a Macro-Roughness Element on Tsunami Wave Amplification, Pressures, and Loads: Physical Model and Comparison to Japanese and US Design Equations

Tori Tomiczek[*],[§], Adi Prasetyo[†],[¶], Nobuhito Mori[†],[‖],
Tomohiro Yasuda[†],[‡],[**] and Andrew Kennedy[*],[††]

[*]*University of Notre Dame, USA*

[†]*Kyoto University, Japan*

[‡]*Kansai University*

[§]*johnvict@oregonstate.edu*

[¶]*adi.prasetyo246@yahoo.com*

[‖]*mori@oceanwave.jp*

[**]*tomo@oceanwave.jp*

[††]*Andrew.B.Kennedy.117@nd.edu*

Experiments were conducted at a 1:20 length scale in a large tsunami flume to measure wave evolution and pressures on and around structural elements. The water surface profiles of waves propagating across a bare beach were compared with those recorded in front of an onshore obstacle representing an urban macro-roughness element. The addition of a structure significantly changed the water surface profile for broken waves: the water surface amplification in the presence of a macro-roughness element reached seven times the bare-earth water surface elevation. Estimated pressures from design equations were calculated using recommended inputs and compared with pressures recorded by gauges installed on the structural elements. Design equations showed good agreement for non-breaking wave pressures but underestimated peak pressures for breaking waves. Likewise, force integrations of measured pressures on the experimental specimen indicated that design equations may underestimate loads due to waves that break offshore and propagate across

a beach as a turbulent bore. The time-integrated pressure impulse was shown to be less sensitive to wave characteristics than the peak recorded pressures. Time-averaged loading curves were also developed for different average periods.

*Keywords*: Tsunami design; bare-earth simulation; JCO; ASCE7; pressure impulse; time-averaged load.

## 1. Introduction

Tsunamis pose significant threats to coastal communities worldwide: recent tsunamis that have caused major damage in coastal regions include the Indian Ocean Tsunami (2004), the South Pacific Tsunami (2009), and the Tohoku Earthquake Tsunami (2011). The 26 December 2004 Indian Ocean Tsunami generated waves up to 30 m that left over 230,000 people dead or missing and caused extensive damage in countries bordering the Indian Ocean [see for example Dalrymple and Kriebel, 2005; Papadopoulos *et al.*, 2006; Tsuji *et al.*, 2006; Koshimura *et al.*, 2009; Leone *et al.*, 2011]. The 29 September 2009 South Pacific Tsunami and the 27 February 2010 Chilean Tsunami also caused substantial damage and loss of life in local villages [see Reese *et al.*, 2011; Mas *et al.*, 2012]. On 11 March 2011, the Tohoku Earthquake Tsunami caused severe damage to over 400,000 homes and catastrophic loss of life along the east coast of Japan [see Mimura *et al.*, 2011; Mori *et al.*, 2011; Udo *et al.*, 2012; Suppasri *et al.*, 2013]. The magnitude and extent of damage were surprising given Japan's extensive history of tsunamis and the sophisticated tsunami countermeasures and warning systems in the country [Zaré and Afrouz, 2012]. To ensure the safety and vitality of coastal communities, local and national governments across the globe must evaluate their tsunami response and preparedness plans to adequately protect citizens and defend structures from damage, especially from beyond-design basis events.

Tsunami behavior on shore can vary depending on local bathymetries and the point of tsunami generation. A tsunami propagating over a submerged reef or a broad coastline may break, becoming an undular bore that dissolves into a chain of solitons in a process known as soliton fission [Brühl and Oumeraci, 2010; Grilli *et al.*, 2012]. Shoreward-propagating turbulent bores may be characterized by a steep, rapidly moving wave front. On beaches with steep slopes, tsunamis may create a gradual rise and fall of the water level; rarely, a tsunami will break right at shoreline and generate a series of very large breaking waves [Yeh, 2009]. The Tohoku Earthquake Tsunami of 2011 was characterized by leading short, peaky waves with a long tail [Kawai *et al.*, 2012]. Tsunami characteristics can change depending on the shape of the tsunami profile from wave to flow. As a result, the tsunami-induced loads can also change from that by impulsive wave-loading to that by a quasi-hydrostatic force. Moreover, the onshore effects of these waves will vary depending on local characteristics and tsunami countermeasures, which include warning systems and evacuation plans as well as groupings of structures or other large obstacles, termed

here macro-roughness elements, that affect wave propagation [Irish *et al.*, 2014; Thomas *et al.*, 2015].

Post-disaster field surveys are useful in evaluating the effectiveness of the design and construction of tsunami mitigation structures. However, it is difficult to estimate hydrodynamic conditions and the resulting loads from survey data; therefore, many reconnaissance-based fragility functions derived from damage surveys assume that the entire tsunami-induced load is based on the maximum water depth [see Reese *et al.*, 2011; Mas *et al.*, 2012; Suppasri *et al.*, 2013]. Numerical models such as COUL-WAVE [Lynett *et al.*, 2002] and NHWAVE [Ma *et al.*, 2012] have simulated tsunami events over real topographies and given useful estimates of inundation, runup, and current velocities. Recent fragility models have included such numerical simulations of current velocity and hydrodynamic force in structural vulnerability models [see Suppasri *et al.*, 2011]. However, individual damage depends on local building structure and design, even under the same hydrodynamic conditions. Moreover, wave-structure interaction is difficult to model [Petukhin *et al.*, 2012], and many models remove buildings to allow for more efficient calculations [see Westerink *et al.*, 2008; Parsons *et al.*, 2014; Yao *et al.*, 2014; Grilli *et al.*, 2015]. Such simplifications can result in errors in hydrodynamic outputs. While margins of error for the majority of recent hurricane storm surge levels modeled by ADCIRC have been reported to be within 0.5 m [Dietrich *et al.*, 2012], numerically hindcast wave-heights can be subject to larger error. For example, after Hurricane Ike affected the Bolivar Peninsula (2008), modeled wave-heights were shown to be greater than those measured by USGS wave gauges by over 1 m in several locations, particularly at locations far from the shoreline; this overprediction affected wave and surge fragility functions derived for pile-elevated residences [Tomiczek *et al.*, 2014]. Tsunami models have also reported that inundation predictions can be overestimated due to coarse grid resolution and smoothed topographies [Parsons *et al.*, 2014; Oishi *et al.*, 2015]. A more thorough understanding of wave propagation through urban environments will enhance the validity and robustness of tsunami simulations.

In addition to numerical modeling, laboratory experiments provide valuable datasets of tsunami propagation. Recent laboratory experiments have measured tsunami-induced water surface elevations, velocities, and pressures on and around structures and on scale models of cities, and physical models have also tested the reliability of tsunami protection structures [see Fujima *et al.*, 2009; Bradner *et al.*, 2009; Hsiao and Lin, 2010; Thomas and Cox, 2012; Park *et al.*, 2013]. However, many previous experiments idealized the tsunami profile using a solitary wave [see Cox *et al.*, 2008; Thomas and Cox, 2012; Park *et al.*, 2013]; this solitary wave model has been shown to scale poorly to prototype tsunami time scales [Madsen *et al.*, 2008]. While work has been done to better represent these tsunami time scales using sine waves or long, leading depression N-waves [see Goseberg, 2013; Allsop *et al.*, 2008; Rossetto *et al.*, 2011; Allsop *et al.*, 2014; Bremm *et al.*, 2015], real tsunami events have shown complex water surface profiles that involve both slow and fast water

level increases [Fujima *et al.*, 2009; Kawai *et al.*, 2012; Goseberg *et al.*, 2013]. There-fore, laboratory experiments that can combine both slow and quick rise mechanisms will help to better understand the hydrodynamics associated with these complex tsunami signals.

Previous laboratory measurements of tsunami-induced pressures have recorded short duration pressure peaks corresponding with wave impact and a following quasi-hydrostatic pressure [see Fujima *et al.*, 2009; Bradner *et al.*, 2009; Thomas and Cox, 2012]. While conducting scale model experiments on highway bridge superstruc-tures, Bradner *et al.* [2009] found that for large-inertia structures the impulse pres-sure may not translate to a slamming force on structural supports. However, these pressures must not be neglected for nonengineered or low-inertia structures. Addi-tionally, wave breaking processes cause complex nonlinear interactions with coastal structures; these turbulent impacts and the accompanying large peak pressures can generate debris and may cause significant structural damage on a localized scale. Previous experiments have noted wide variations in impact pressures under identi-cal wave conditions; therefore, it is difficult to relate wave conditions to expected peak pressures [Chan and Melville, 1988]. The pressure impulse, defined as the time integral of the pressure peak, has been used to characterize violent wave impacts, because it has shown greater consistency and less sensitivity to the shape of the wave immediately before impact than the maximum pressure [Cooker and Peregrine, 1995; Peregrine, 2003]. The energy transferred when a wave impacts a vertical wall is reflected and may be observed as a water jet accelerating vertically up the wall [Cooker and Peregrine, 1995]. This water jet increases inundation and damage, and it corroborates the need for numerical and physical models to include wave-structure interaction for reliable estimations of structural vulnerability.

Historical damage data, numerical simulations, and laboratory experiments are used by local and national governments to create tsunami mitigation practices for vulnerable regions. These practices include developing tsunami warning and evacuation systems for residents and improving design equations for coastal struc-tures. Raby *et al.* [2015] provide a thorough overview of Japanese, American, and British design guidelines for sea defense structures. It is important to analyze stan-dards for both tsunami-mitigation structures and residential structures to validate their applicability to real world events. For example, the American Society of Civil Engineers (ASCE) and the Japanese Cabinet Office (JCO) provide equations to estimate the maximum pressures and loads caused by a tsunami based on the max-imum tsunami inundation depth, $h_{max}$. This depth is an important consideration in tsunami design; however, due to the complexity of recent tsunami profiles and the processes associated with the interaction of a tsunami wave with a coastal struc-ture, inputs into design equations are subject to error. Design equations must make simplifying assumptions in order to be applicable to a wide range of coastal devel-opments and wave characteristics; both the ASCE [2016] and JCO [2005] equa-tions assume that $h_{max}$ is the maximum depth at the structure's location with

no obstacle affecting tsunami propagation, termed the "bare-earth" water surface elevation.

Using benchmark experimental data obtained at Kyoto University's Hybrid Tsunami Open Flume in Ujigawa (HyTOFU), this assumption was analyzed by comparing the peak water surface elevations recorded by onshore wave gauges for varying tsunami wave conditions with and without the presence of a single macro-roughness element. Using these water surface elevation measurements, peak pressures and loads predicted by design equations were compared with those measured by gauges mounted on an experimental specimen. Section 2 provides a description of the design standards evaluated, and Sec. 3 describes the instrumentation and experimental methods for data collection. Section 4 presents the results of the experiment, contrasting water surface elevation measurements with and without obstacles and comparing experimental pressure measurements with those obtained using standards. Load calculations using distributions given in design standards are also compared with integrated forces from experimental pressure gauges, and time-averaged loads are presented, which may apply to structural response times. Finally, Sec. 5 summarizes the major findings of this work and presents engineering recommendations for tsunami load estimation.

## 2. Design Standards

The design equation proposed by the JCO [2005] is based on a series of laboratory experiments performed by Asakura *et al.* [2000] on two-dimensional scale models. From these experiments, Asakura *et al.* [2000] empirically estimated the maximum tsunami loading as a triangular distribution with base pressure, $p_{max}$, equal to three times the hydrostatic pressure [see Fig. 1(a)]; that is,

$$p_{max} = 3\rho g h_{max}, \tag{1}$$

where $\rho$ and $g$ are the density of water and the acceleration due to gravity, respectively. In Eq. (1), $h_{max}$ is taken as the height of the bore at the structure, without considering splash or other phenomena associated with wave-structure interaction. This equation has been examined for its applicability to real tsunami events and other flume experiments. For example, Nakano [2008] observed damage after the Indian Ocean Tsunami disaster and calculated a coefficient, $\alpha$, for Eq. (1) by assuming the tsunami pressure was equal to the lateral resistance of a damaged home at an elevation, $z$, above ground level:

$$p'_{max} = \rho g(\alpha h_{max} - z). \tag{2}$$

Nakano [2008] found that $\alpha = 3$ was reasonably able to distinguish between damaged and surviving structures, but drifting debris and other environmental factors may make Eq. (1) less conservative. Similar evaluations of Eq. (1) have been performed experimentally [see Fujima *et al.*, 2009; Achmed *et al.*, 2009] and alternative
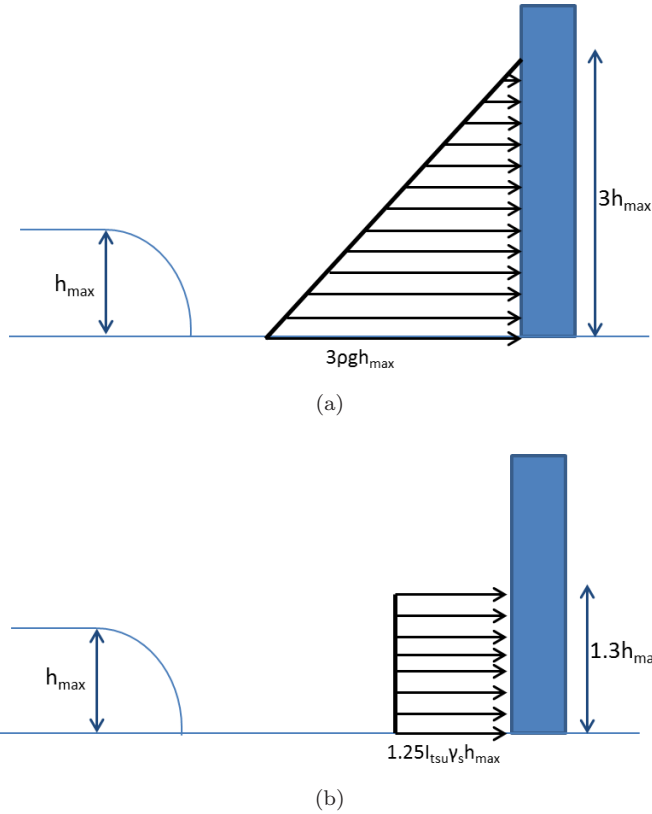
(a)



(b)

Fig. 1. Design vertical tsunami pressure distribution, recommended by (a) Japanese Cabinet Office [2005] and (b) American Society of Civil Engineers [2016].

coefficients have been suggested. Still, Eq. (1) remains the standard in Japan for tsunami design, although much research has been done to improve its formulation to include flow effects [see Kihara *et al.*, 2015]. Using this design pressure, the maximum force per unit width, $F_{\max}/W$, may then be estimated by applying a triangular distribution over a height $3h_{\max}$ :

$$\frac{F_{\max}}{W} = 4.5\rho g h_{\max}^2 \tag{3}$$

Prior to 2011, a US standard for designing structures to resist tsunami effects did not exist [ASCE, 2014]. This circumstance was partially because the US has experienced fewer damaging tsunamis than other regions in the Pacific Ocean. The most destructive tsunami affecting the West Coast of North America to date was the 1964 Great Alaska Earthquake Tsunami, which caused damage and loss of life in Alaska, California, Oregon, and British Columbia [Parsons *et al.*, 2014]. However, many areas of the US remain vulnerable to damage by earthquake-generated tsunamis. Therefore, in early 2011, the ASCE formed a subcommittee to develop the first U.S. tsunami loading standard. These standards will be published in ASCE

7–16 as a new chapter [ASCE, 2014; Raby *et al.*, 2015; ASCE, 2016] and have been developed for the Pacific Coast of the US. The guidelines include tsunami hazard maps for Alaska, the Pacific Coast, and Hawaii, and the chapter provides procedures for estimating tsunami inundation, runup, flow characteristics, and hydrostatic and hydrodynamic loads [ASCE, 2016]. Equation 6.10.1-1 of ASCE 7 [2016] estimates the combination of the unbalanced lateral hydrostatic and hydrodynamic loads caused by a tsunami as:

$$p_{\max} = 1.25 I_{tsu} \gamma_s h_{\max}, \tag{4}$$

where $p_{\max}$ is the simplified equivalent uniform lateral static pressure. In Eq. (4), $I_{tsu} = 1.0$ or $1.25$ based on the Importance Factor of the structure and $\gamma_s$ is the minimum fluid weight density for hydrostatic loads, equal to 1.1 times the specific weight of seawater. Substituting conservative coefficients such that $I_{tsu} = 1.25$ and $\gamma_s = 1.1\,\rho g$, Eq. (4) may be reformulated to resemble Eq. (1):

$$p_{\max} = 1.72 \rho g h_{\max}. \tag{5}$$

Comparison of Eqs. (1) and (5) implies that the design pressure estimated using ASCE [2016] is less conservative than that obtained using JCO [2005]. Note also in Fig. 1(b) that ASCE [2016] recommends a different pressure distribution when estimating the tsunami-induced force on a structure, applying $p_{\max}$ uniformly over 1.3 times the inundation depth in the direction of flow. This distribution leads to a force per unit width estimate of:

$$\frac{F_{\max}}{W} = 2.23 \rho g h_{\max}^2. \tag{6}$$

Therefore, ASCE [2016] loads are less than those estimated by JCO [2005] by a factor of two.

## 3. Instrumentation and Experimental Conditions

HyTOFU measures $45\,\text{m} \times 4\,\text{m} \times 2\,\text{m}$ deep; plan and profile views of the flume may be seen in Fig. 2. The flume is capable of three types of wave generation: a mechanical piston capable of producing a solitary wave with height up to $0.5\,\text{m}$, a $70\,\text{kW}$ pump that can produce constant flow rates from $0$–$0.833\,\text{m}^3/\text{s}$, and volumetric tank that can vertically discharge a constant volume of water from a set elevation above the free surface in an analogy to a dam break mechanism. Generation mechanisms may be used individually or in combination to create complex wave profiles. In this experiment, a constant flow rate was generated for $60\,\text{s}$ before the mechanical paddle was used to create a wave that propagated $14.05\,\text{m}$ across a flat bathymetry with initial water depth $h_0 = 0.700\,\text{m}$, up a $7.95\,\text{m}$ long 1:10 planar slope, and across a flat beach to the end of the flume.
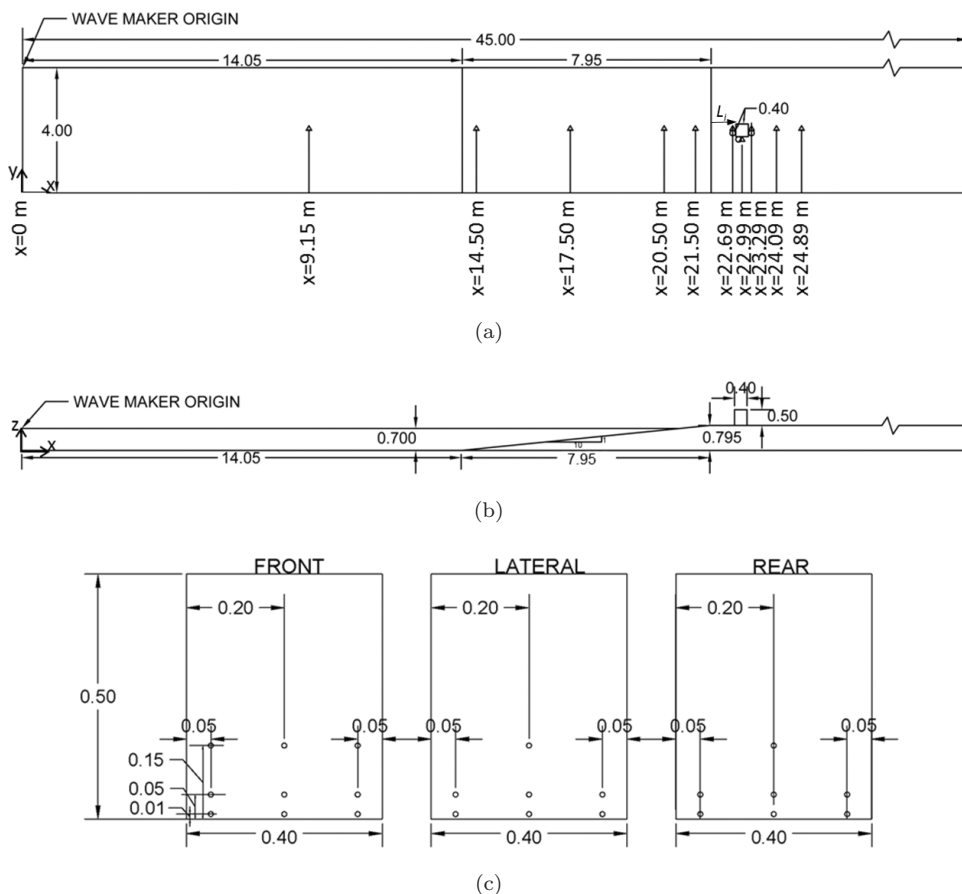
Fig. 2. Hydraulic Flume (a) plan and (b) profile. (c) Schematic of pressure sensors installed on the front face of the structural element.

Based on flume dimensions, a 1:20 length scale and Froude Number similitude were chosen for experiments. Offshore water surface perturbations from 0.40 m to 0.48 m were representative of prototype waves with amplitudes between 8 and 9.6 m, and the dimensions of the structural element (0.4 m × 0.4 m × 0.5 m tall) corresponded with those of a narrow Japanese house with base dimensions 8 m × 8 m. Placing the macro-roughness element in the flume resulted in an increased blocking ratio, which caused greater wave reflection and an increased drag coefficient. This effect caused slightly increased water surface elevations in the offshore as well as flow amplification in the side channels due to flow constriction. Additionally, this effect caused lower water surface elevations in areas directly shielded by the macro-roughness element. Trials with multiple structural elements in the flume showed that structures shielded by one or more rows of obstacles experienced lower pressures than unshielded structures [Tomiczek *et al.*, 2016]. Thus, results presented here apply to unshielded structures impacted by a tsunami wave.

Figure 2(a) shows wave gauge distances ($x$) from the mechanical paddle and the obstacle positioned a distance $L_i = L_1 = 0.79\,\text{m}$ from the start of the horizontal beach. Four configurations were tested: one with no onshore obstacles and three with the front edge of the macro-roughness element positioned a distance ($L_i$) from the beginning of the horizontal beach. The three distances tested were: $L_1 = 0.79\,\text{m}$ ($x = 22.79\,\text{m}$ from the wavemaker origin), (b) $L_2 = 1.59\,\text{m}$ ($x = 23.59\,\text{m}$) or (c) $L_3 = 2.39\,\text{m}$ ($x = 24.39\,\text{m}$). To evaluate the effects of the macro-roughness element on the variation of the onshore water surface profile, the water surface elevation time series directly in front of the structure was compared for experiments with and without the obstacle.

The water surface elevation time series was recorded using wire resistance wave gauges; in wave generation, mechanical and pumping inputs were chosen to create waves with similar total offshore water surface perturbations, ($\eta_{\text{wave}} + \eta_{\text{flow}}$), but varied contributions due to pumping flow and solitary wave, which affected onshore wave transformation and breaking conditions. Table 1 shows the seven combinations of mechanically generated waves and pump-generated flow rates used for experiments, as well as the ensemble average and standard deviation of the total water surface perturbation. The contribution to the total water surface perturbation by the mechanically generated wave was defined as $\eta_{\text{wave}}$ and that from the constant pumping flow was defined as $\eta_{\text{flow}}$; as seen in Table 1, trials ranged from constant pump flow (resulting in a large $\eta_{\text{flow}}$ and $\eta_{\text{wave}} = 0$) to a nearly pure solitary wave with minimal pumping input (resulting in $\eta_{\text{wave}}$ nearly equal to ($\eta_{\text{wave}} + \eta_{\text{flow}}$)). Figure 3 shows the water surface profiles at six distances from the mechanical paddle origin for the bare-earth configuration and the definitions for $\eta_{\text{wave}}$ and $\eta_{\text{flow}}$. Note in Fig. 3 that each water surface profile $\eta_i$ refers to the water surface perturbation measured for the corresponding trial in Table 1. As shown in the figure, from Trial 1 to Trial 7, the combinations of pumping and mechanical wave inputs created waves with similar total offshore water surface perturbations but increasing contribution from the solitary wave and decreasing contribution from pumping flow. Trials with large pumping flows (large $\eta_{\text{flow}}$) may be thought to represent a hurricane-induced

Table 1. Combinations of mechanically generated wave and constant pumping flow characteristics and maximum water surface perturbation at $x = 14.50\,\text{m}$.

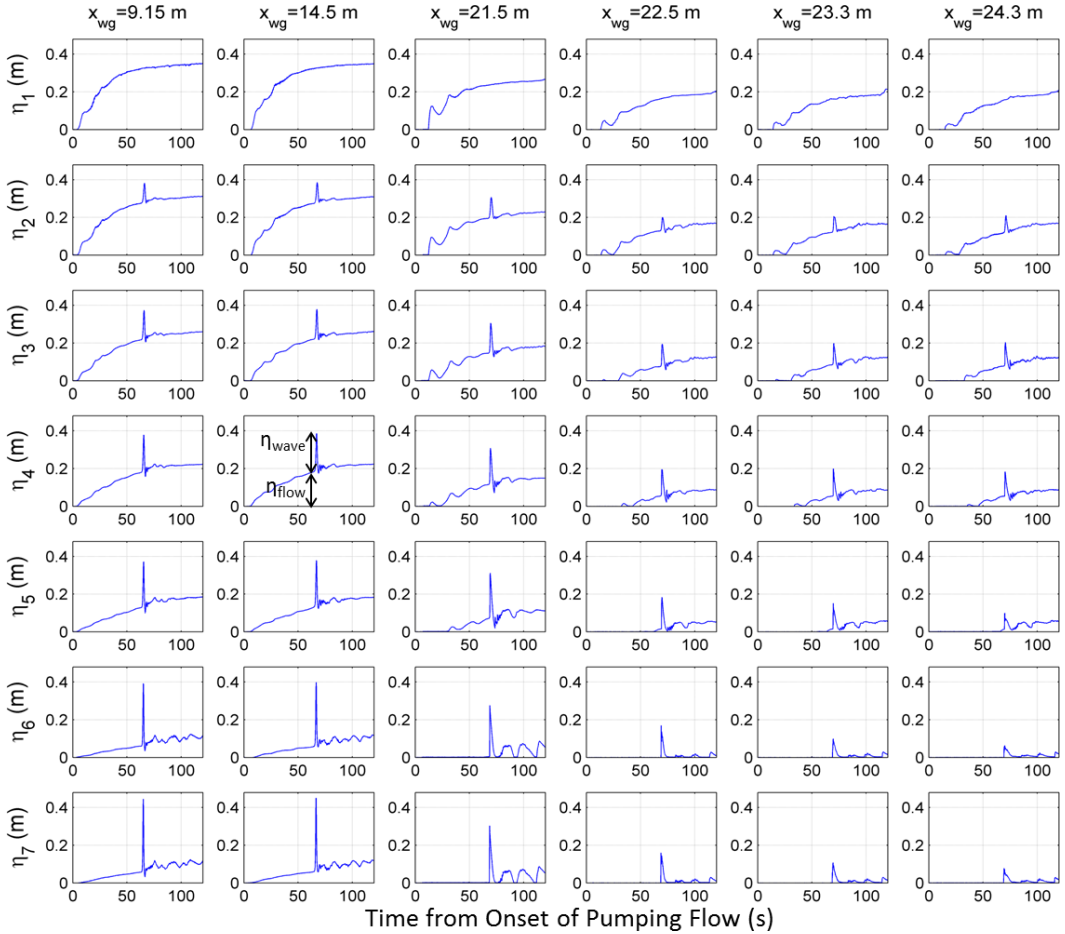| Trial | Target Soliton Wave Input (m) | Pump Constant Flow Input (m$^3$/s) | $(\overline{\eta_{\text{wave}} + \eta_{\text{flow}}})$ (m) $x = 14.50\,\text{m}$ | Standard deviation (cm) |
|---|---|---|---|---|
| 1 | 0 | 0.80 | 0.4085 | 0.0010 |
| 2 | 0.10 | 0.60 | 0.4129 | 0.0014 |
| 3 | 0.15 | 0.40 | 0.3980 | 0.0027 |
| 4 | 0.20 | 0.30 | 0.4026 | 0.0012 |
| 5 | 0.25 | 0.20 | 0.3961 | 0.0016 |
| 6 | 0.35 | 0.10 | 0.4194 | 0.0012 |
| 7 | 0.40 | 0.10 | 0.47789 | 0.0016 |

Fig. 3. Water surface perturbations ($\eta$) at distances ($x_{wg}$) from the mechanical paddle for the seven combinations of mechanical and pumping inputs tested. Each subscript ($i$) of $\eta_i$ refers to the numbered trial listed in Table 1.

storm surge or a tsunami that causes a constant rise and fall of water level. Trials 6 and 7 were shown to successfully recreate the tsunami profile recorded by offshore GPS Buoys during the 2011 Tohoku Earthquake Tsunami [Tomiczek *et al.*, 2016]. Although the period of a solitary wave, when scaled, is less than that of a prototype tsunami [Madsen *et al.*, 2008], trials in which $\eta_{\text{wave}} > \eta_{\text{flow}}$ are still important for comparison with design equations that estimate the total tsunami-induced force on a structure based only on the maximum tsunami height.

Each of the seven trials listed in Table 1 was generated twice for each experimental set up to check the repeatability of wave characteristics, giving a total of eight iterations of each trial. As seen in Table 1, the standard deviation of water surface elevations at $x = 14.50$ m from the wavemaker origin ranged from 0.001 to 0.003 cm for individual trials, indicating that wave conditions were very repeatable and thus could confidently be compared for different distances $L_i$. Comparison of all trials

indicates that Trials 1–6 produced an offshore ($x = 14.50\,\text{m}$) total water surface perturbation between $0.395\,\text{m}$ and $0.420\,\text{m}$, while Trial 7 produced a total water surface perturbation 17.6% larger than other trials with ($\overline{\eta_{\text{wave}} + \eta_{\text{flow}}} = 0.479\,\text{m}$).

Figure 2(c) shows the locations of the 50 kPa-rated pressure gauges, manufactured by Kyowa Co. Ltd., that were mounted on the front, lateral, and rear sides of the structural element to measure the impact and following quasi-hydrostatic pressures. As seen in the figure, nine pressure gauges were positioned on the front face of the structural element in three rows of three at elevations $0.01\,\text{m}$, $0.05\,\text{m}$, and $0.15\,\text{m}$. On the side and back faces, seven pressure gauges were positioned in two rows of three at elevations $0.01\,\text{m}$ and $0.05\,\text{m}$, with one gauge located at elevation $0.15\,\text{m}$ along the centerline of the structure. Sensitivity tests recorded pressure data at 200 Hz, 500 Hz, and 1000 Hz and verified that a 200 Hz sampling frequency was sufficient to capture the magnitude of the short-duration impulsive pressure peaks; thus, to optimize the efficiency of the recording software, the 200 Hz frequency was selected for data collection. Data were checked for contamination by local utility frequencies (60 Hz) using a low pass filter for frequencies less than 50 Hz. Cleaned data was checked for sensitivity to higher frequency components, and filtered peak pressure recordings differed by less than 5% from unfiltered data.

## 4. Results and Discussion

### 4.1. *Water surface amplification by structures*

Figure 4 shows a comparison of the water surface elevation time series with and without the structure for setback distances $L_2 = 1.59\,\text{m}$ and $L_3 = 2.39\,\text{m}$ for the wave of Trial 7 in Table 1. The control, bare-earth time series in Fig. 4 indicates that the wave propagated past both locations with a very low water surface elevation $\eta_{\text{be}}$; visual observation and video analysis of the trial confirmed that the wave broke near the crest of the slope and propagated along the flat beach as a turbulent bore with a high propagation speed. As seen in Fig. 4, adding a structure significantly changed the water surface profile when the wave propagated past the location of interest. The collision of the wave with the structure created a large vertical jet that was nearly five times the height of the water surface elevation with no obstacle present when at setback distance $L_2$ and over seven times that at distance $L_3$. Trials with the obstacle positioned at both distances $L_2$ and $L_3$ showed wave amplification due to wave-structure interaction; however, the wave gauge in front of the obstacle positioned further inland recorded a larger amplification despite having a lower peak water surface elevation when the wave propagated across the no-obstacle topography. Therefore, the difference between the true water surface profile and that predicted by bare-earth numerical models may be larger at inland distances affected by waves that still contain a great amount of energy. As tsunamis lose energy moving inland due to breaking, turbulence generated around obstacles, and overland friction, waves are expected to create smaller reflected jets when they come into contact with a rigid
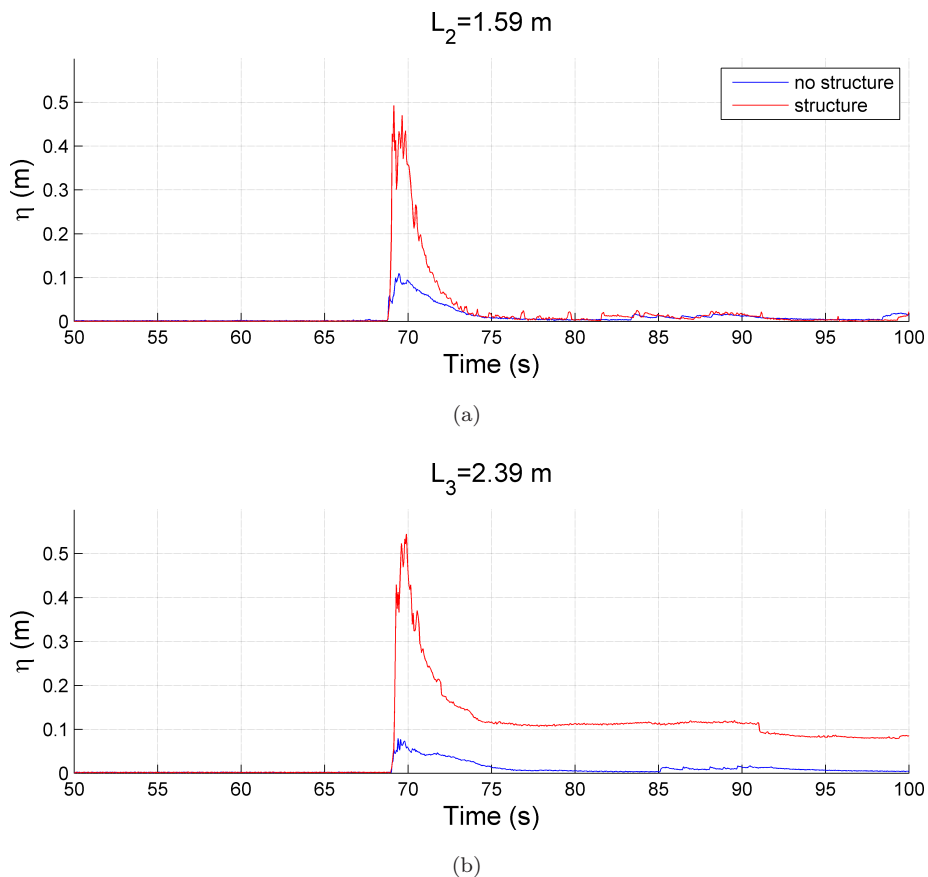
## $L_2$=1.59 m



(a)

## $L_3$=2.39 m



(b)

Fig. 4. (Color online) Time series of water surface elevation for Trial 7 at distances (a) $L_1 =$ 1.59 m (b) $L_2 = 2.39$ m over bare-earth topography (blue line) and with a macro-roughness element positioned in the flume (red line).

structure. Therefore, after a certain distance inland, error in numerical simulations should decrease with increasing distance from shore.

Trial 7 was generated by the largest mechanical wave input (0.40 m target wave-height) and the smallest pumping flow input (0.10 m³/s). Other trials considered waves with increased flow rates and decreased mechanical solitary wave inputs. To parameterize these varying wave conditions, the offshore solitary wave fraction, $\eta*$, was defined as the ratio of the mechanically generated wave perturbation, $\eta_{\text{wave}}$, to the total water surface perturbation above the stillwater depth caused by both the constant flow and the mechanical wave, ($\eta_{\text{wave}} + \eta_{\text{flow}}$):

$$\eta^* = \frac{\eta_{\text{wave}}}{\eta_{\text{wave}} + \eta_{\text{flow}}}. \tag{7}$$

As the wave profile approaches that of a solitary wave, with no constant-flow contribution to the water level increase, $\eta*$ approaches 1. For pure pumping conditions in which the water level steadily increases but no mechanical wave is generated, both

$\eta_{\text{wave}}$ and $\eta*$ become 0. This constant flow, $\eta* = 0$ condition can be equated to the slow water level rise associated with a storm surge generated by a tropical cyclone.

In experiments, waves with large pumping flow inputs corresponded to those with small solitary wave fractions ($\eta* < 0.5$); these waves did not break on the obstacle. Breaking waves are associated with more violent wave impacts on structures [see Cooker and Peregrine, 1995; Bullock *et al.*, 2007]; thus the maximum obstacle-induced water surface amplification was expected to occur for larger values of $\eta*$. This hypothesis was confirmed by comparing the maximum water surface elevation including a macro-roughness element, $\eta_{\text{mr}}$, to the bare-earth water surface profile, $\eta_{\text{be}}$. The ratio $\eta_{\text{mr}}/\eta_{\text{be}}$ was plotted against $\eta*$ for Trials 1–7 of Table 1 for distances $L_2$ and $L_3$ in Fig. 5. For both setback distances, increasing values of $\eta*$ corresponded with larger water surface amplification ratios. As $\eta*$ approached 1, $\eta_{\text{mr}}/\eta_{\text{be}}$ increased rapidly. Note that increasing the obstacle setback distance from 1.59 m to 2.39 m increased the water surface amplification ratio for Trials 6 and 7. However, positioning the obstacle a large enough distance from shore such that waves have lost a significant amount of energy is expected to reduce the water surface amplification caused by wave-structure interaction.

### 4.2. *Comparison with design standards*

As discussed above, design equations for estimating the maximum tsunami-induced pressure often use the bare-earth water surface elevation in front of the structure without accounting for wave-structure interaction. Equations (1) and (5) were evaluated using the water surface elevations recorded in the bare-earth trial, and estimated pressures were compared with the peak pressures recorded during experiments. Figure 6 shows the pressures predicted by design equations, nondimensionalized by the bare-earth hydrostatic pressure, plotted against $\eta*$ at the elevations of experimental pressure gauges. The corresponding peak pressures measured by each of the three front gauges at the corresponding elevation are also plotted for distances $L_1, L_2$, and $L_3$. As seen in the figure, taking $h_{\text{max}}$ as the no-obstacle water surface
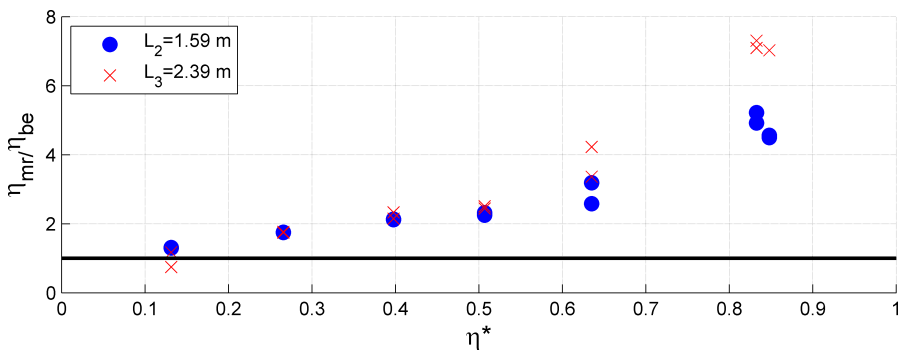


Fig. 5. Ratio of maximum water surface elevation with the obstacle ($\eta_{\text{mr}}$) to that without the macro-roughness element ($\eta_{\text{be}}$), for distances $L_2$ ($\bullet$) and $L_3$ ($x$).
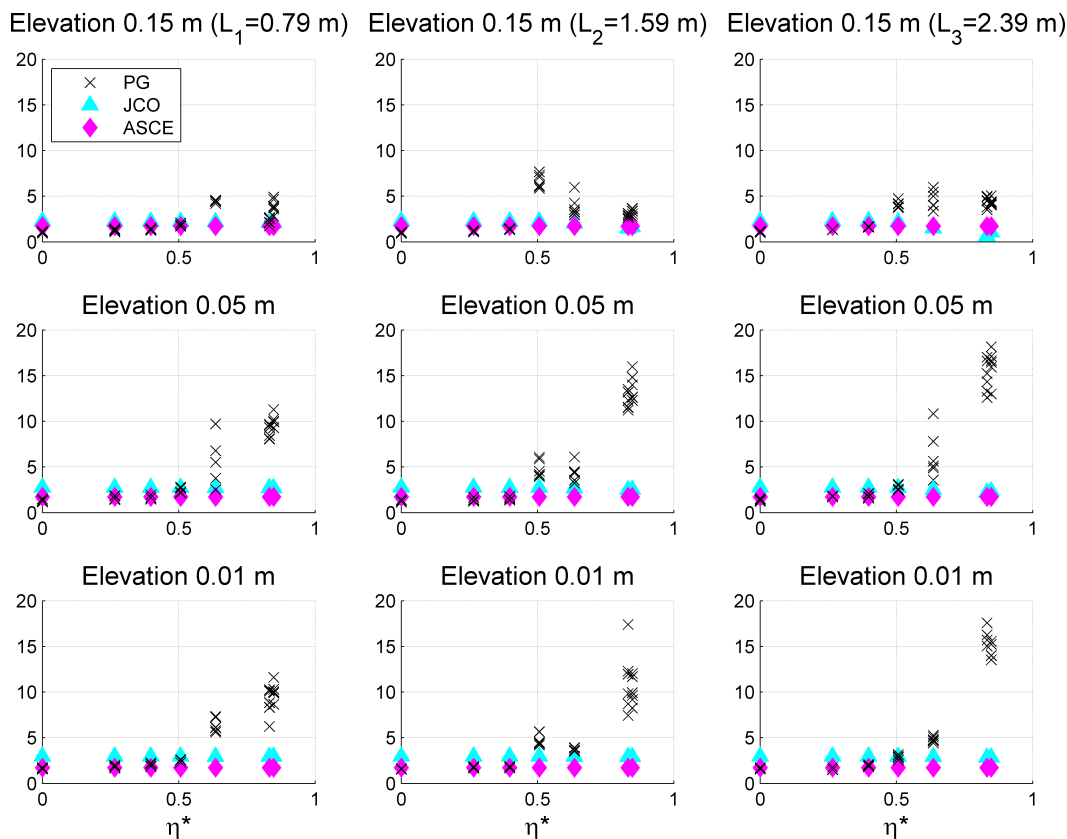
Fig. 6. Normalized peak pressure: measured ($x$), JCO (▲) or ASCE (♦), versus $\eta*$ at elevations 0.15 m (top), 0.05 m (middle), and 0.01 m (bottom) above the base of the structure for setback distances $L_1$ (left), $L_2$ (middle), and $L_3$ (right).

elevation resulted in good agreement between predicted and measured pressures for non-breaking wave conditions. However, after wave breaking, disregarding the water surface amplification caused by wave-structure interaction generally underestimated measured peak pressures, especially for pressure gauges located near the base of the structure. For example, for breaking waves, measured pressures were three times as high as those predicted by Eq. (1) and five times as high as those obtained from Eq. (5) at distance $L_1$; distances $L_2$ and $L_3$ showed even larger differences. Equation (1) was a factor of 5 times smaller than measured values at distance $L_2$ and 7.3 times smaller at distance $L_3$, while Eq. (5) underpredicted experimental pressures by a factor of 9.1 at distance $L_2$ and 12.9 at distance $L_3$. Better understanding of the environmental conditions at a structure and the processes associated with wave impact may give more reliable estimations of expected peak pressures and loads on coastal structures.

Because peak impulsive pressures are associated with wave breaking, when designing a building component to resist these critical pressures, coastal engineers

must consider a structure's location from shore and the wave characteristics, which determine the horizontal inland position of wave breaking. As discussed above, current design equations do not include wave-structure interaction in $h_{\max}$ inputs for pressure determinations; therefore, depending on the condition, they may underestimate peak pressures as shown in Fig. 6. While it is useful to compare pressure estimations directly, most design codes are written to resist the total load on a structure; both the ASCE [2016] and JCO [2005] provide pressure distributions for estimating the total force caused by a tsunami wave. Therefore, the respective force estimates of Eqs. (3) and (6) were applied to estimate the JCO [2005] and ASCE [2016] design loads, and these load estimations were compared with integrations of experimental pressures on each face of the structure. To estimate the maximum force on the macro-roughness element, pressure measurements were integrated to create an envelope of potential forces by using assumptions that yielded an upper and lower-limit force. The face of the structural element was divided into three subsections; the pressure measured by a gauge at a given elevation was assumed to be constant over the width of its subsection. Pressures gradients were assumed to be linear between vertical gauges; therefore, instantaneous loads were estimated via a combination of triangular and trapezoidal distributions. The upper-limit force estimation assumed a hydrostatic pressure between the top pressure gauges ($z = 0.15$ m) and the point of zero pressure; while the lower bound assumed that all pressures above $z = 0.15$ m were zero. The rear force was calculated in a similar manner, with trapezoidal distributions of pressure gauge measurements at 0.01 m and 0.05 m elevations and assuming the pressure at the gauge elevated at 0.15 m was constant across the width of the structure. For each trial, the front and rear forces were calculated, and the total force was determined by subtracting the rear force from the front force.

A comparison of experimentally determined and design-based loads, nondimensionalized by the bare-earth hydrostatic force, may be seen in Fig. 7. For each trial, the front, rear, and total forces are plotted against $\eta*$. As shown in the figure, the rear force for all wave conditions gave a negligible contribution to the total force on the structure. Therefore, for further analyses presented here, the frontal force is considered as a critical force to account for potential damage to a sea facing wall or other element. However, for cases involving multiple obstacles (such as a coastal community), where reflection is likely to create wave impact on the rear side of a structure, this rear force may be amplified and should be accounted for in coastal design. Comparing the experimental load integrations with those predicted by the JCO [2005] and ASCE [2016] equations indicates that design equations perform well for non-breaking waves ($\eta* < 0.5$), giving conservative estimates that agree with experimental loads. However, as the solitary wave fraction approached one, design equations tended to underestimate even the lower bound peak force integrations. Therefore, modifications to design equations are recommended to account for a wave's impulsive force on a structure.
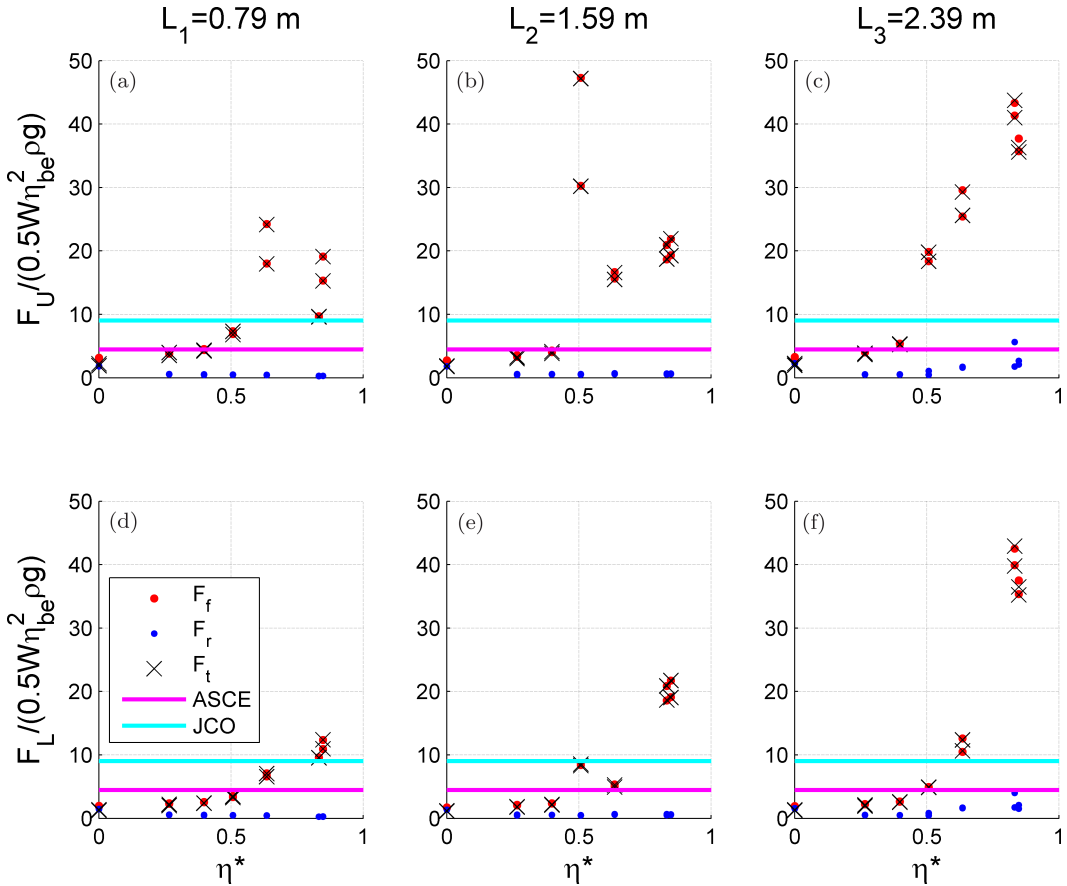
Fig. 7. (a, b, and c): upper and (d, e, and f) lower-bound force integrations: front (●), rear (●), and total (x), normalized by the bare-earth hydrostatic force, at each setback location.

It is important to note that upper-bound experimental forces are extrapolations; more reliable force estimations would be obtained with additional pressure sensors installed on the experimental specimen, particularly at elevations higher than 0.15 m. Additionally, there remains some debate as to whether the large pressure peaks and resulting loads associated with wave impact need to be included in the design of large-inertia structures due to their short duration [Bradner *et al.*, 2009]. Nevertheless, when considering small-inertia structures or localized damage to house components, these large impulsive pressures should not be neglected.

### 4.3. Pressure impulse and characteristic time-scale loading

Impulsive pressure is significant if a wave breaks near an obstacle, although its duration time is very short. For example, Cooker and Peregrine [1995] noted that laboratory experiments may record pressures that are significantly larger than those in the field, and peak pressures may vary for breaking waves at a given location.

Witte [1988] showed that even regular waves cause impact pressures that can vary significantly; this variability in impact pressure was shown in later experiments to be largely due to the shape of the breaker [Oumeraci *et al.*, 1993; Hattori *et al.*, 1994]. The current experiment also showed that pressures varied significantly with a changing solitary wave fraction; thus, the maximum pressure on a structure is strongly influenced by the shape of the incoming wave. One way to reduce the variability of the pressure peaks is to calculate the total pressure impulse, $P(x)$, by integrating the pressure time series, $p(x, t)$, over the duration of the impact, $dt$:

$$P(x) = \int_{tb}^{ta} p(x, t)dt, \tag{8}$$

where $t_b$ is the time before impact and $t_a$ is the time after impact [Cooker and Peregrine, 1995; Lamb, 1995].

The pressure impulse has shown consistency for waves of known characteristics [Bagnold, 1939] and may be significant when analyzing the lifecycle fragility of a coastal structure to repeated wave impacts. However, pressure impulse is difficult to quantify, because the definition of the integration boundaries $t_b$ and $t_a$ in pressure impulse calculations are subject to the somewhat arbitrary choice of the scientist [Wood *et al.*, 2000]. In experiments of aerated and nonaerated violent breaking wave impacts on vertical and sloping walls, Bullock *et al.* [2007] defined $t_b$ as the initial point at which a wave-induced force rose above the noise level and $t_a$ as the first point after which the peak pressure fell below the maximum quasi-hydrostatic force. Wood *et al.* [2000] used a similar definition for $t_a$ and identified the start of impact as the intersection of the pressure time series with a horizontal line projected from the maximum quasi-hydrostatic pressure. Following the definition of Bullock *et al.* [2007], $t_b$ and $t_a$ were selected as shown in Fig. 8, and the area under the pressure time series was integrated to calculate the pressure impulse for each trial listed in Table 1 for setback distances $L_2$ and $L_3$. Note that impulsive pressure is characterized by its short time duration: depending on level of aeration involved in the wave-structure collision, the total time span of an impulsive pressure is typically between $0.08\,\text{s}$ and $0.45\,\text{s}$ [Bullock *et al.*, 2007]. The first three trials of Table 1 involved large pumping rates, and the mechanically generated wave propagated past the obstacle unbroken. Under these conditions, the pressure sensors did not record an impulsive pressure spike, but rather a gradual rise and fall of pressure that agreed reasonably with an equivalent hydrostatic pressure calculated from the water surface elevation. Therefore, the pressure impulse was not calculated for trials involving large flow and non-breaking waves.

The effects of varying offshore wave conditions on changing the peak pressure and pressure impulse were analyzed by calculating dimensionless parameters as follows:

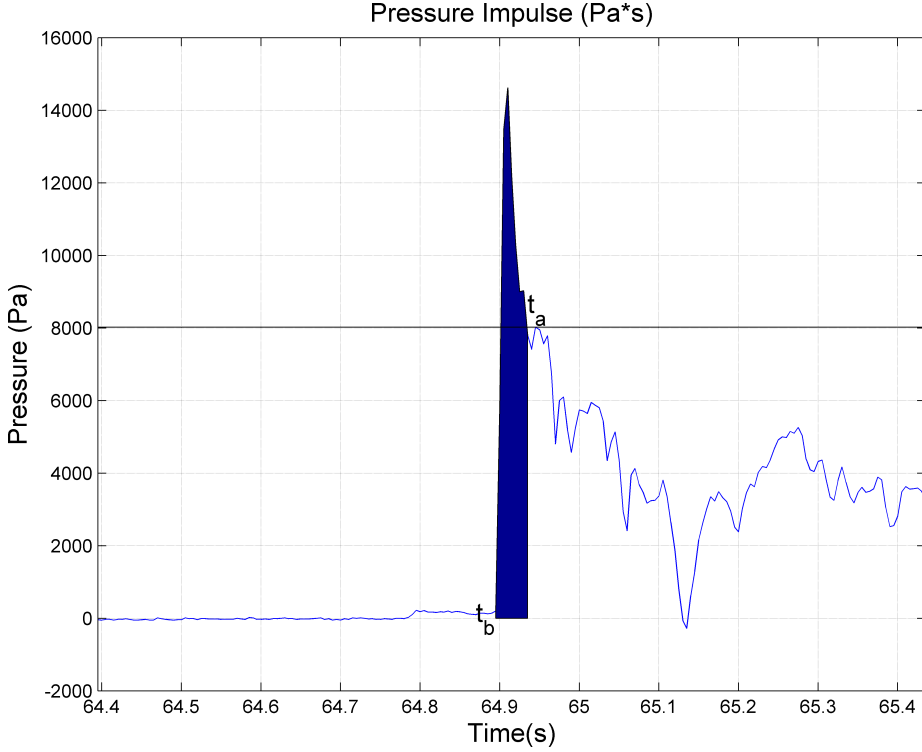$$p_{\max}^* = \frac{p_{\max}}{\rho g(\eta_{\text{wave}} + \eta_{\text{flow}})}, \tag{9}$$

Fig. 8. Definition of pressure impulse. The pressure time series was integrated from the beginning of the pressure rise $(t_b)$ to the time that a horizontal line projected from the point of maximum quasi-hydrostatic pressure $(-)$ first intersected the time series after the peak pressure $(t_a)$.

and

$$P* = \frac{P}{\rho g(\eta_{\text{wave}} + \eta_{\text{flow}})T_{\text{wave}}}. \tag{10}$$

In the above equations, $p*_{\text{max}}$ and $P*$ represent the dimensionless peak pressure and dimensionless pressure impulse, respectively. The offshore solitary wave rise time, $T_{\text{wave}}$, and total water surface perturbation were measured at $x_{WG} = 14.50\,\text{m}$ from the mechanical paddle. $T_{\text{wave}}$ was determined manually for each trial based on the wave gauge time series, with the start and end of the wave determined as the points at which the water surface profile crossed a horizontal line extending through $\eta_{\text{flow}}$. Note that $T_{\text{wave}}$ approaches infinity for the constant flow condition $(\eta* = 0)$; however, the pressure impulse, $P$, and its corresponding dimensionless parameter, $P*$, are relevant for breaking and broken wave conditions. Dimensionless values are plotted for each value of the solitary wave ratio in Fig. 9 for setback distances $L_2$ and $L_3$. Non-breaking waves $(\eta* < 0.5)$ were characterized by peak pressures similar to the offshore hydrostatic pressure measured $14.50\,\text{m}$ from the wavemaker. Although no pressure impact peak was recorded for non-breaking waves, note that these wave-flow combinations induced greater water depths affecting the
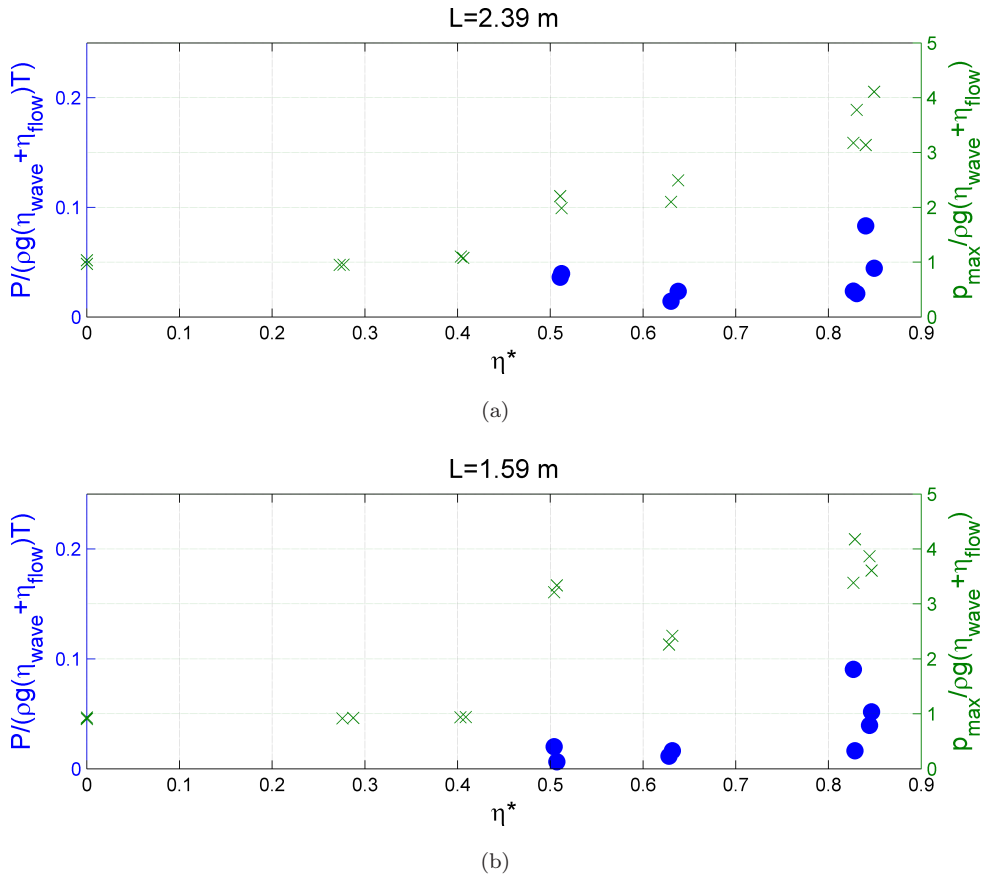
Fig. 9. Normalized pressure impulse (left axes, •) and peak pressure (right axes, x) versus offshore solitary wave fraction for obstacle placed (a) 2.39 m and (b) 1.59 m from the horizontal beach.

structure for longer periods of time. Therefore, although the maximum pressures recorded for non-breaking waves were less than those measured in trials involving larger solitary waves, the duration and magnitude of these pressures may contribute to fatigue failure or failure due to time-dependent phenomena such as foundation scour. Thus, these quasi-hydrostatic pressures are significant design considerations. Breaking waves, on the other hand, showed relatively consistent pressure impulse values with increasing $\eta*$, as has been observed in previous experiments [see Bagnold, 1939; Peregrine, 2003]. This consistency may be contrasted with the dimensionless peak pressure, which increased as $\eta*$ approached 1. Therefore, the pressure impulse may be more robustly estimated by numerical models of wave propagation over topographies with urban roughness effects than the peak pressure itself; if set up correctly, these computational fluid dynamics models may successfully reproduce the pressure time series due to wave impact. Future work must standardize the definitions of the beginning and end of the pressure peak. By integrating the pressure

time series over this defined duration, a characteristic pressure impulse may be characterized for a given wave condition. Because the characteristic pressure impulse has not previously been included in design standards, care must be taken to incorporate this quantity as a useful value for engineers to identify a range of peak pressures affecting a structure.

The total pressure impulse is important for lifecycle fragility analysis or when analyzing the vulnerability of a bridge or other large-inertia structure. Thus, a way to parameterize a characteristic loading time scale for wave impacts may be useful in the design of structures with known response periods in order to resist failure due to fatigue as well as critical loading. Figure 10 shows the time-averaged force integrations plotted against the averaging duration, $T*$, with $T^* = \dfrac{dt}{\sqrt{\eta_{be}/g}}$. Loads obtained from design standards are shown as horizontal lines, because time scales are not considered in Eqs. (3) and (6). Non-breaking wave conditions impose similar forces over all time scales, while breaking waves, ($\eta* > 0.51$), tend to exceed estimations by design standards, particularly at short time scales. As seen in the figure, time-averaged loads tend to decrease and approach constant values as $T*$ increases for non-breaking and broken wave conditions. Therefore, design equations
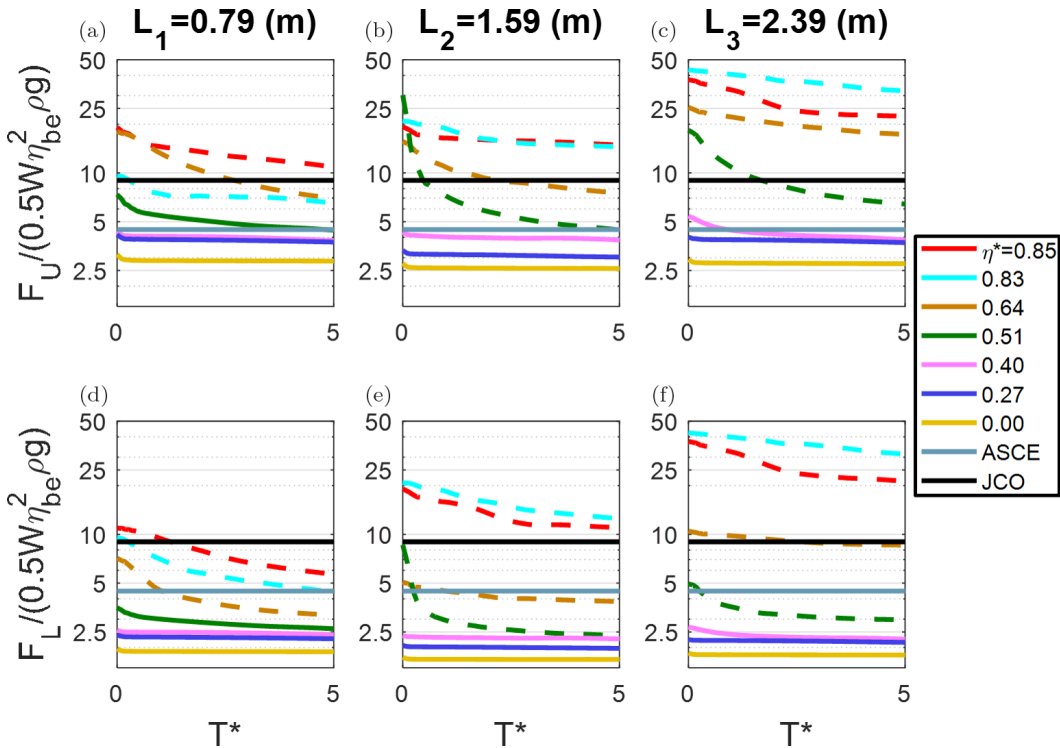


Fig. 10. Upper- (a, b, and c) and lower- (d, e, and f) bound force estimations versus normalized averaging time for $L_1$ (a and d), $L_2$ (b and e) and $L_3$ (c and f). Breaking conditions (dotted lines) exceed standards-based force estimations.

for structures built to resist longer time scale loads may consider including conservative safety factors to estimate the maximum force based on the expected wave climate. However, when considering localized damage to structural components, an engineer may consider the peak pressure associated with breaking waves.

## 5. Summary and Conclusions

Experiments conducted at Kyoto University's Hybrid Tsunami Open Flume in Ujigawa generated a general dataset for a simple structural setup and showed that the presence of an idealized macro-roughness obstacle significantly affected onshore wave propagation by changing the water surface profile compared to a bare-earth configuration. Results identified important trends for both non-breaking and breaking wave interactions with structures. Key findings from this work are threefold:

1. The water surface elevations of waves propagating across a bare beach were significantly different than those measured when obstacles were positioned onshore, especially for waves that broke before the obstacle and propagated across the beach as high velocity, low-elevation bores. Urban macro-roughness elements may therefore cause errors in numerical models that calculate water surface elevations and velocities using the post-event, bare-earth topography of a region. The horizontal location of the structure and the solitary wave fraction were shown to be important parameters influencing wave propagation and dissipation. For breaking waves, the difference between the bare-earth water surface elevation and that affected by a macro-roughness element increased when the obstacle was positioned further from shore. Thus, compared to field measurements, water surface elevations obtained from bare-earth numerical models are hypothesized to have significant errors in front of structures impacted by waves propagating with a great deal of energy. As waves lose energy moving very far inland, error in numerical models should likewise decrease, although this has not been definitively proven in this work. Additional wave tests for obstacles positioned at further setback distances will provide better understanding about wave transformation and dissipation.

2. Using bare-earth water surface elevations in ASCE [2016] and JCO [2005] design equations yielded pressures that agreed with measured peak pressures for non-breaking waves. However, these bare-earth inputs for $h_{max}$ significantly underestimated measured peak pressures for breaking waves, especially at pressure gauges elevated 0.01 m above the base of the structure. Likewise, estimates of the total force on the obstacle using the ASCE [2016] or JCO [2005] equations were generally conservative for non-breaking waves but underestimated force integrations of recorded pressures for breaking waves.

3. For breaking waves, the time-integrated pressure impulse showed more consistency for trials with varying solitary wave fractions than did the impulsive peak

pressure. Design equations that can estimate time-averaged loads may be useful for the design of structures with known response periods.

In practice, a coastal engineer must account for case-specific parameters associated with local bathymetry, community layout, and offshore wave characteristics. In addition, due to the short duration of the very large impact pressures measured here, conservative designs to withstand these peak pressures should be applied to structures of significant community importance, and more research is required to fully understand the effects of impulsive breaking wave loads on coastal structures. However, coastal structures must be designed to resist all loads generated by tsunamis, which include wave impacts on structural components, debris impact, and other uncertainties. Engineers, city planners, and residents must work together to understand the full effects of macro-roughness elements on wave propagation in order to find cost-effective, innovative design techniques that prepare coastal communities to robustly withstand future tsunami events.

## Acknowledgments

## References

Achmed, F., Shigihara, Y., Fujima, K. & Mizutani, N. [2009] "Experimental study on tsunami forces: Estimation of tsunami force acting on structures related to run up distance, scale of building and pressure distribution," in *Proc. 5th International Conf. Asian and Pacific Coasts*, 13–18 October 2009. Singapore, pp. 114–121.

Allsop, W., Robinson, D., Charvet, I., Rossetto, T. & Abernathy, R. [2008] "A unique tsunami generator for physical modelling of violent flows and their impact," in *Proc. 14th World Conference 32 on Earthquake Eng.*, October, Beijing, pp. 1–8.

Allsop, W., Chandler, I. & Zaccaria, M. [2014] "Improvements in the physical modelling of tsunamis and their effects," in *Proc. of the 5th International Conference on the Application of Physical Modelling to Port and Coastal Protection*, September-October, Bulgaria.

Asakura, R., Iwase, K. & Iketani, T. [2000] *Proc. Coastal Eng. JSCE* **47**, 911–915.

ASCE [2014] "New chapter on tsunami design in ASCE 7-16," *ASCE*. ASCE, 23 January 2014. Web. 20 October 2015. Available at http://www.asce.org/structural-engineering/news/20140123-new-chapter-on-tsunami-design-in-asce-7-16/.

ASCE [2016] "Minimum design loads for buildings and other structures," in *ASCE/SEI 7–16* (in preparation of publication).

Bagnold, R. A. [1939] "Interim report on wave pressure research," *J. Insti. Civil Eng.* **12**, 202–226.

Bradner, C., Schumacher, T., Cox, D. & Higgins, C. [2009] "Large scale laboratory measurements of wave forces on highway bridge superstructures," in *Proc. 31st Int.*, Hamburg, Germany, pp. 3554–3566.

Bremm, G. C., Goseberg, N., Schlurmann, T. & Nistor, I. [2015] "Long wave flow interaction with a single square structure on a sloping beach," *J. Marine Sci. Eng.* **3**, 821–844.

Brühl, M. & Oumeraci, H. [2010] "Analysis of soliton fission over a submerged structure using 'Nonlinear Fourier Transform (NLFT),'" *Coastal Eng. Proc.* **32**, 1–12.

Bullock, G. N., Obhrai, C., Peregrine, D. H. & Bredmose, H. [2007] "Violent breaking wave impacts. Part 1: Results from large-scale regular wave tests on vertical and sloping walls," *Coast. Eng.* **54**, 602–617.

Chan, E. S. & Melville, W. K. [1988] "Deep-water plunging wave pressures on a vertical plane wall," *Proc. R. Soc. London. A* **417**, 95–131.

Cooker, M. J. & Peregrine, D. H. [1995] "Pressure impulse theory for liquid impact problems," *J. Fluid Mech.* **297**, 193–214.

Cox, D., Tomita, T., Lynett, P. & Holman, R. A. [2008] "Tsunami inundation with macroroughness in the constructed environment," *ASCE*, pp. 1421–1432.

Dalrymple, R. A. & Kriebel, D. L. [2005] "Lessons in engineering from the tsunami in Thailand," *Bridge* **35**(2), 4–13.

Dietrich, J. C., Tanaka, S., Westerink, J. J., Dawson, C. N., Luettich Jr., Zijlema, M., Holthuijsen, L. H., Smith, J. M., Westerink, L. G. & Westerink, H. J. [2012] "Performance of the unstructured-mesh, SWAN+ADCIRC Model in computing hurricane waves and surge," *J. Sci. Comput.* **52**, 468–497.

Fujima, K., Achmad, F., Shigihara, Y. & Mizutani, N. [2009] "Estimation of tsunami force acting on rectangular structures," *J. Disast. Res.* **4**(6), 404–409.

Goseberg, N. [2013] "Reduction of maximum tsunami run-up due to the interaction with beachfront development-application of single sinusoidal waves," *Nat. Hazards Earth Syst. Sci.* **13**, 2991–3010.

Goseberg, N., Wurpts, A. & Schlurmann, T. [2013] "Laboratory-scale generation of tsunami and long waves," *Coast. Eng.* **79**, 57–74.

Grilli, S., Harris, J. C., Shi, F., Kirby, J. T., Tajalli Bakhsh, T. S., Estibals, E. & Tehranirad, B. [2012] "Numerical modeling of coastal tsunami dissipation and impact," *Coastal Eng. Proc.* **33**, 1–12.

Grilli, S., O'Reilly, C., Harris, J., Bakhsh, T. T., Tehranirad, B., Banihashemi, S., Kirby, J., Baxter, C., Eggeling, T., Ma, G. & Shi, F. [2015] "Modeling of SMF tsunami hazard along the upper US East Coast: Detailed impact around Ocean City, MD," *Nat. Hazards* **76**, 705–746.

Hattori, M., Arami, A. & Yui, T. [1994] "Wave impact pressure on vertical walls under breaking waves of various types," *Coast. Eng.* **22**(1–2), 779–114.

Hsiao, S. & Lin, T. [2010] "Tsunami-like solitary waves impinging and overtopping an impermeable seawall: Experiment and RANS modeling," *Coast. Eng.* **57**, 1–18.

Irish, J., Weiss, R., Yang, Y., Song, Y. K., Zainali, A. & Marivela-Colmenarejo, R. [2014] "Laboratory experiments of tsunami run-up and withdrawal in patchy coastal forest on a steep beach," *Nat. Hazards* **74**, 1933–1949.

JCO/Task Committee under the Japanese Cabinet Office. [2005] "Design Guidelines for Tsunami Shelters" (in Japanese), Available at http://www.bousai.go.jp/oshirase/h17/ tsunami_s iryo 2.pdf.

Kawai, H., Satoh, M., Kawaguchi, K. & Seki, K. [2012] "Recent tsunamis observed by GPS buoys off the Pacific coast of Japan," *Coast. Eng. Proc.* **33**, 1–15.

Kihara, N., Niida, Y., Takabatake, D., Kaida, H., Shibayama, A. & Miyagawa, Y. [2015] "Large-scale experiments on tsunami-induced pressure on a vertical tide wall," *Coast. Eng.* **99**, 46–63.

Koshimura, S., Oie, T., Yanagisawa, H. & Imamura, F. [2009] "Developing fragility functions for tsunami damage estimation using numerical model and post-tsunami data from Banda Aceh, Indonesia," *Coast. Eng. J.* **51**(3), 243–273.

Lamb, H. [1995] *Hydrodynamics*, 6th edn. (Cambridge University Press, New York).

Leone, F., Lavigne, F., Paris, R., Denain, J. C. & Vinet, F. [2011] "A spatial analysis of the December 26th, 2004 tsunami-induced damages: Lessons learned for a better risk assessment integrating buildings vulnerability," *Appl. Geography.* **31**(1), 363–375.

Lynett, P., Wu, T. & Liu, P. [2002] "Modeling wave runup with depth-integrated equations," *Coast. Eng.* **46**, 89–107.

Ma, G., Shi, F. & Kirby, J. T. [2012], "Shock-capturing non-hydrostatic model for fully dispersive surface wave processes," *Ocean Modelling* **43–44**, 22–35.

Madsen, P. A., Fuhrman, D. R. & Schaffer, H. A. [2008] "On the solitary wave paradigm for tsunamis," *J. Geophys. Res.* **113**, C12012, doi: 10.1029/2008JC004932.

Mas, E., Koshimura, S., Suppasri, A., Matsouka, M., Matsuyama, M., Yoshii, T., Jimenez, C., Yamazaki, F. & Imamura, F. [2012] "Developing Tsunami fragility curves using remote sensing and survey data of the 2010 Chilean Tsunami in Dichato," *Nat. Hazards* **12**, 2689–2697.

Mimura, N., Yasuhara, K., Kawagoe, S., Yokoki, H. & Kazama, S. [2011] "Damage from the Great East Japan Earthquake and Tsunami- A quick report," *Mitigation Adaptation Strategies Global Change* **16**(7), 803–818.

Mori, N., Takahashi, T., Yasuda, T. & Yanagisawa, H. [2011] "Survey of 2011 Tohoku earthquake tsunami inundation and run-up," *Geophys. Res. Lett.* **38**(7), L00G14.

Nakano, Y. [2008] "Design load evaluation for tsunami shelters based on damage observations after Indian Ocean Tsunami disaster due to the 2004 Sumatra Earthquake," *The 14th World Conference on Earthquake Engineering*, 12–17 October, Beijing, pp. 1–8.

Oishi, Y., Imamura, F. & Sugawara, D. [2015] "Near-field tsunami inundation forecast using the parallel TUNAMI-N2 model: Application to the 2011 Tohoku-Oki earthquake combined with source inversions," *Geophys. Res. Lett.* **42**, 1083–1091.

Oumeraci, H., Klammer, P. & Partenscky, H. W. [1993] "Classification of breaking wave loads on vertical structures," *J. Waterw. Port Coast. Ocean Eng.* **119**(4), 381–397.

Papadopoulos, G. A., Caputo, R., McAdoo, B., Pavlides, S., Karasthis, V., Fokaefs, A., Orfanogiannaki, K. & Valkaniotis, S. [2006] "The large tsunami of 26 December 2004: Field observations and eyewitnesses accounts from Sri Lanka, Maldives Is. and Thailand," *Earth Planets Space* **58**(2), 233–241.

Park, H., Cox, D. T., Lynett, P. J., Wiebe, D. M. & Shin, S. [2013] "Tsunami inundation modeling in constructed environments: A physical and numerical comparison of free-surface elevation, velocity, and momentum flux," *Coast. Eng.* **79**(2), 9–21.

Parsons, T., Geist, E., Ryan, H., Lee, H., Haeussler, P., Lynett, P., Hart, P., Sliter, R. & Roland, E. [2014] "Source and progression of a submarine landslide and tsunami: The 1964 Great Alaska earthquake at Valdez," *J. Geophys. Res. Solid Earth* **119**, 8502–8516.

Peregrine, D. H. [2003] "Water wave impacts on walls," *Annu. Rev. Fluid Mech.* **35**, 23–43.

Petukhin, A., Yoshida, K. & Miyakoshi, K. [2012] "Tsunami simulation for the 2011 Great Tohoku earthquake (Mw9.0), Japan, using seismic inversion source model and fully nonlinear tsunami model," *Fifteenth World Conf. Earthquake Engineering*, Lisboa, pp. 1–9.

Raby, A., Macabuag, J., Pominis, A., Wilkinson, S. & Rossetto, T. [2015] "Implications of the 2011 Great East Japan Tsunami on sea defense design," *Int. J. Disaster Risk Reduct.* **14**(2015), 332–346.

Reese, S., Bradley, B. A., Bind, J., Smart, G., Power, W. & Sturman, J. [2011] "Empirical building fragilities from observed damage in the 2009 South Pacific tsunami," *Earth-Sci. Rev.* **107**(1–2), 156–173.

Rossetto, T., Allsop, W., Charvet, I. & Robinson, D. I. [2011] "Physical modelling of tsunami using a new pneumatic wave generator," *Coast. Eng.* **58**(6), 517–527.

Suppasri, A., Koshimura, S. & Imamura, F. [2011] "Developing tsunami fragility curves based on the satellite remote sensing and the numerical modeling of the 2004 Indian Ocean tsunami in Thailand," *Nat. Hazards Earth Syst. Sci.* **11**, 173–189.

Suppasri, A., Mas, E., Charvet, I., Gunasekera, R., Imai, K., Fukutani, Y., Abe, Y. & Imamura, F. [2013] "Building damage characteristics based on surveyed data and fragility curves of the 2011 Great East Japan tsunami," *Nat. Hazards* **66**, 319–341.

Thomas, S. & Cox, D. [2012] "Influence of finite-length seawalls for tsunami loading on coastal structures," *J. Waterw. Port Coast. Ocean Eng.* **138**(3), 203–214.

Thomas, S., Killian, J. & Bridges, K. [2015] "Influence of Macroroughness on Tsunami loading of coastal structures," *J. Waterw. Port Coast. Ocean Eng.* **141**(1), 1–14.

Tomiczek, T., Kennedy, A. B. & Rogers, S. [2014] "Collapse limit state fragilities of wood-framed residences from storm surge and waves during Hurricane Ike," *J. Waterw. Port Coast. Ocean Eng.* **140**(1), 43–55.

Tomiczek, T., Prasetyo, A., Mori, N., Yasuda, T. & Kennedy, A. B. [2016] "Physical modelling of tsunami onshore propagation, peak pressures, and shielding effects in an urban building array," *Coastal Eng.* **117**, 97–112.

Tsuji, Y., Namegaya, Y., Matsumoto, H., Iwasaki, S. I., Kanuba, W., Sriwachai, M. & Meesuk, V. [2006] "The 2004 Indian tsunami in Thailand: Surveyed runup heights and tide gauge records," *Earth Planets Space* **58**(2), 223–232.

Udo, K., Sugawara, D., Tanaka, H., Imai, K. & Mano, A. [2012] "Impact of the 2011 Tohoku Earthquake and Tsunami on beach morphology along the Northern Sendai Coast," *Coast. Eng. J.* **54**(1), 1250009.

Westerink, J. J., Luettich, R. A., Feyen, J. C., Atkinson, J. H., Dawson, C., Roberts, H., Powell, M. D., Dunion, J. P., Kubatko, E. J. & Pourtaheri, H. [2008] "A basin-to channel-scale unstructured grid hurricane storm surge model applied to southern Louisiana," *Monthly Weather Rev.* **136**(3), 833–864.

Witte, H. H. [1988] "Wave induced impact loading in deterministic and stochastic reflection," *Mitt Leichtweiss Inst. Wasserbau*, Tech. Univ. Braunschweig **102**, 1–227.

Wood, D. J., Peregrine, D. H. & Bruce, T. [2000] "Wave impact on a wall using pressure-impulse theory. I: Trapped air," *J. Waterw. Port Coast. Ocean Eng.* **126**(4), 182–190.

Yao, Z., Kennedy, A. B., Aaron S. Donahue, Westerink, J. J., Panda, N. & Dawson, C. [2014] "Rotational surf zone modeling for O( mu4) Boussinesq-Green-Naghdi systems," *Ocean Modeling* **79**, 43–53.

Yeh, H. [2009] "Tsunami impacts on coastlines," in *The Sea*: *Tsunamis.* eds. Bernard, E. N. & Robinson, A. R. (Harvard University Press, Cambridge), pp. 333–370.

Zaré, M. & Afrouz, S. G. [2012] "Crisis management of Tohoku; Japan Earthquake and Tsunami, 11 March 2011," *Iranian J. Public Health* **41**(6), 12–20.